PNAS RESEARCH ARTICLE | APPLIED PHYSICAL SCIENCES OPEN ACCESS

Mechanism for plasmon-generated solvated electrons

Alexander Al-Zubeidi[a,b], Behnaz Ostovar[b,c], Claire C. Carlin[b,d], Boxi Cam Li[b,e], Stephen A. Lee[a,b], Wei-Yi Chiang[a,b,1], Niklas Gross[a,b], Sukanya Dutta[a,b], Anastasiia Misiura[a,b], Emily K. Searles[a,b], Amrita Chakraborty[a,b], Sean T. Roberts[b,e,2], Jennifer A. Dionne[b,f,g,2], Peter J. Rossky[a,b,h,2], Christy F. Landes[a,b,c,h,2], and Stephan Link[a,b,h,2]

Edited by George Schatz, Northwestern University, Evanston, IL; received October 5, 2022; accepted December 7, 2022

Solvated electrons are powerful reducing agents capable of driving some of the most energetically expensive reduction reactions. Their generation under mild and sustainable conditions remains challenging though. Using near-ultraviolet irradiation under low-intensity one-photon conditions coupled with electrochemical and optical detection, we show that the yield of solvated electrons in water is increased more than 10 times for nanoparticle-decorated electrodes compared to smooth silver electrodes. Based on the simulations of electric fields and hot carrier distributions, we determine that hot electrons generated by plasmons are injected into water to form solvated electrons. Both yield enhancement and hot carrier production spectrally follow the plasmonic near-field. The ability to enhance solvated electron yields in a controlled manner by tailoring nanoparticle plasmons opens up a promising strategy for exploiting solvated electrons in chemical reactions.

nanoparticles | hot carriers | hydrated electrons | photoemission

Solvated electrons serve as potent reducing agents in organic synthesis and have attracted renewed attention for their promise in challenging reactions like CO_2 and organohalide reduction, ammonia production, and waste treatment (1–10). Their solution-phase nature allows them to act as homogenous reactants, thereby overcoming the limitations of heterogeneous catalysis (4, 5). Unlike other homogenous catalysts, they leave no residue upon reaction, making them inherently clean reagents (6). Solvated electrons are traditionally prepared by ionizing radiation or by dissolving alkali metals in a selective set of solvents at cryogenic temperatures (2, 3, 11). However, these conditions produce unwanted radicals or are difficult to work with (1, 2, 6, 12, 13). Recently, the preparation of solvated electrons using continuous-wave visible or near-ultraviolet irradiation of specifically designed solvated electron-producing solids based on upconverting quantum dots or thin diamond films has gained attention as a selective and safe source of solvated electrons with yields of 2×10^{-9} and 6×10^{-3}, respectively (5, 7).

The photoemission of electrons from plasmonic metal nanostructures represents a promising alternate method for generating solvated electrons. Continuous-wave near-ultraviolet irradiation supplies electrons in metal films with enough energy to inject into solution (14, 15). Photoemission occurs through the ejection of a hot electron from the metal produced by the absorption of a photon in the bulk (Fig. 1*A*), or through scattering of a photon with an electron at the metal surface (Fig. 1*B*) (16). Studies in the 1970s found that electron photoemission is enhanced when metals are roughened (15). Because of the close similarity to surface-enhanced Raman scattering (SERS), discovered around the same time, the enhancement has been inferred to arise from localized surface plasmons, the collective oscillation of conduction band electrons (17). The plasmon excitation creates large electric fields at the nanoparticle surface, enhancing not just spectroscopic signals but also the creation of hot carriers in either the metal or its surrounding (18–20). However, the exact role of plasmons in solvated electron generation is still not well understood due to a lack of mechanistic insight, which connects plasmonic near-fields to solvated electron yields.

A major problem is the absence of a detailed correlation of the wavelength-dependent solvated electron yields with the structure-dependent plasmon modes because prior work was carried out on irregularly roughened surfaces without knowledge of nanoscale morphology (15, 17). Intricate control of nanostructured features and advancements in electromagnetic simulations have enabled the field of plasmonics to mature considerably (26–29), leading to the development of SERS as a commercial tool (30, 31) and to the emergence of a variety of photocatalysts based on plasmon-induced hot carriers (32–34). However, while charge transfer from plasmonic nanoparticles into adsorbed molecules (32–35), semiconductors (36, 37), and vacuum (38, 39) have been studied, the emission of electrons into liquids remains largely unexplored despite the advantages of solvated electrons as strong homogeneous catalysts for solution-phase reactions.

Significance

The ideal catalyst for energy-intensive reactions such as CO_2 reduction and waste treatment is non-toxic and sustainable and leaves no unwanted by-products. Solvated electrons, while traditionally prepared by ionizing radiation or by dissolving alkali metals in harsh solvents, are otherwise ideal reducing agents. For the past 50 years, it has been proposed that solvated electrons could be produced by photoexcitation of roughened metal electrodes, but to date no study has demonstrated a clear mechanism for their generation, hindering the optimization and use of solvated electrons as climate-friendly catalysts. Here, we establish this missing link using a combination of electrochemical detection, spectroscopy, structural characterization, and simulations to show that plasmons create solvated electrons in the most sustainable solvent — water.

Author contributions: A.A.-Z., S.T.R., J.A.D., P.J.R., C.F.L., and S.L. designed research; A.A.-Z., B.O., C.C.C., B.C.L., S.A.L., W.-Y.C., N.G., S.D., A.M., and A.C. performed research; A.A.-Z., B.O., C.C.C., B.C.L., S.A.L., W.-Y.C., N.G., S.D., and A.M. analyzed data; E.K.S. designed figures; and A.A.-Z., E.K.S., S.T.R., J.A.D., P.J.R., and S.L. wrote the paper.

The authors declare no competing interest.

This article is a PNAS Direct Submission.

Copyright © 2023 the Author(s). Published by PNAS. This open access article is distributed under Creative Commons Attribution-NonCommercial-NoDerivatives License 4.0 (CC BY-NC-ND).

[1]Present address: Department of Chemistry, National Kaohsiung Normal University, Kaohsiung 80201, Taiwan.

[2]To whom correspondence may be addressed. Email: roberts@cm.utexas.edu, jdionne@stanford.edu, peter.rossky@rice.edu, cflandes@rice.edu, or slink@rice.edu.

This article contains supporting information online at https://www.pnas.org/lookup/suppl/doi:10.1073/pnas.2217035120/-/DCSupplemental.

Published January 10, 2023.

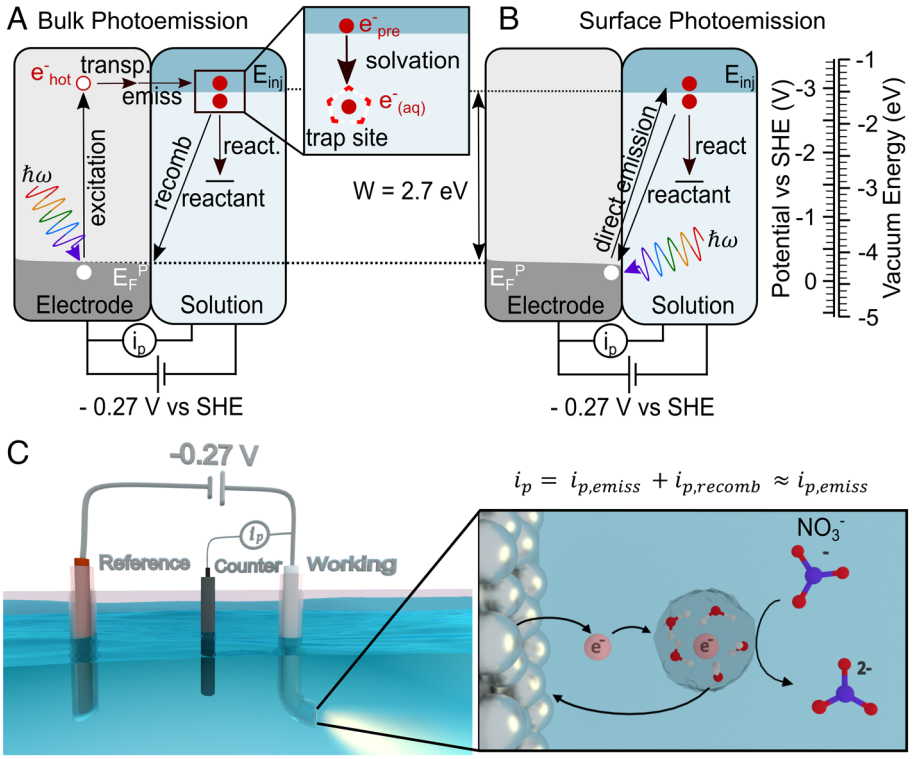

Fig. 1. Detection of solvated electrons generated at metal electrodes. (*A* and *B*) Energy level diagram of electron photoemission into liquids. In bulk photoemission, an electron at the Fermi level, E_F^P, is excited by light, $\hbar\omega$, to form a hot electron, e^-_{hot}, followed by transport to the surface and emission into the electron injection level, E_{inj}, forming first a pre-solvated electron, e^-_{pre}. In surface photoemission, the electron is directly emitted into solution by the collision of an electron at the surface with a photon. W is the photoemission threshold energy. In both cases, the injected electron rapidly relaxes to form a solvated electron e^-_{aq}, which can either react in solution or recombine with the electrode surface (21–24). (*C*) Illustration of photocurrent measurement. Emission of electrons leads to a cathodic photocurrent, $i_{p,emiss}$, whereas recombination of a solvated electron with the electrode gives rise to an anodic current, $i_{p,recomb}$ (15, 17). In the presence of electron scavengers, $i_{p,recomb}$ is suppressed and the measured photocurrent, i_p, can be related to the photoemission quantum yield. In our experiments, various LEDs were employed with power densities between 15 and 700 mW cm^{-2}, 10 to 100 times lower than lasers or arc lamps typically used in plasmon catalysis or electron photoemission studies (5, 7, 25). The excitation light was focused onto an L-shaped working electrode, immersed in an aqueous solution of $NaNO_3$. Unless otherwise stated, a potential of −0.27 V vs. SHE was applied to remove photogenerated holes and fix the electrode Fermi level.

Here we demonstrate that the enhancement of solvated electron production by plasmonic nanostructures originates from the hot carriers that are generated in the bulk metal through plasmon decay. The light-induced injection of electrons into solution leads to a cathodic photocurrent (15, 17), which we relate to photoemission quantum yields (Fig. 1*C*). We compare photoemission yields from polished silver films to nanostructured silver electrodes with well-defined plasmon modes to calculate spectrally resolved enhancement factors that track the plasmonic near-field. Based on the simulations of hot carrier populations and comparison with nanostructured gold electrodes with plasmon resonances at lower photon energies, we assign the enhancement in solvated electron yield to plasmon-induced hot electrons.

Results and Discussion

To establish the viability of quantifying solvated electrons electrochemically, we first collected photoemission-induced photocurrents from polished gold and silver electrodes (Fig. 2*A*), which do not support localized surface plasmons. Cathodic photocurrents at a constant negative potential of –0.27 V were generated with 4.7 eV photons in the presence of nitrate ions that scavenged solvated electrons, preventing them from recombining with the electrode (Fig. 2*B*). As the scavenger concentration was decreased, more electrons recombined with the electrode, lowering the measured photocurrent, in excellent agreement with theory for the homogenous capture of electron injection into solution (Fig. 2*C*) (40) (*SI Appendix*, Fig. S1). Control experiments confirmed that contributions to the photocurrent from photothermal heating, photoinduced electrode charging, and reactions at the electrode surface were negligible (*SI Appendix*, Figs. S2–S5).

Photoemission spectra of polished electrodes demonstrated the energy threshold for injecting electrons into water (Fig. 2*D*). Using the measured light power, P, incident on the electrode surface and the peak photon energy, $\hbar\omega$, of the light-emitting diode (LED), photocurrents, i_p, were first converted into photoemission quantum yields, η_0, to account for differences in photon flux between the LEDs:

$$\eta_0 = \frac{i_p \times \hbar\omega}{P} \quad [1]$$

This probability of an electron leaving the electrode is proportional to the excess energy above the photoemission threshold according to Eq. **2** (14):

$$\eta_0 = A\left[\hbar\omega - \left(E_F^P - E_{inj}\right)\right]^{\frac{5}{2}} = A[\hbar\omega - W]^{\frac{5}{2}} \quad [2]$$

A is a proportionality constant, $\hbar\omega$ is the incident photon energy, E_{inj} is the solvated electron injection level, E_F^P is the electrochemical potential modified electrode Fermi level, and

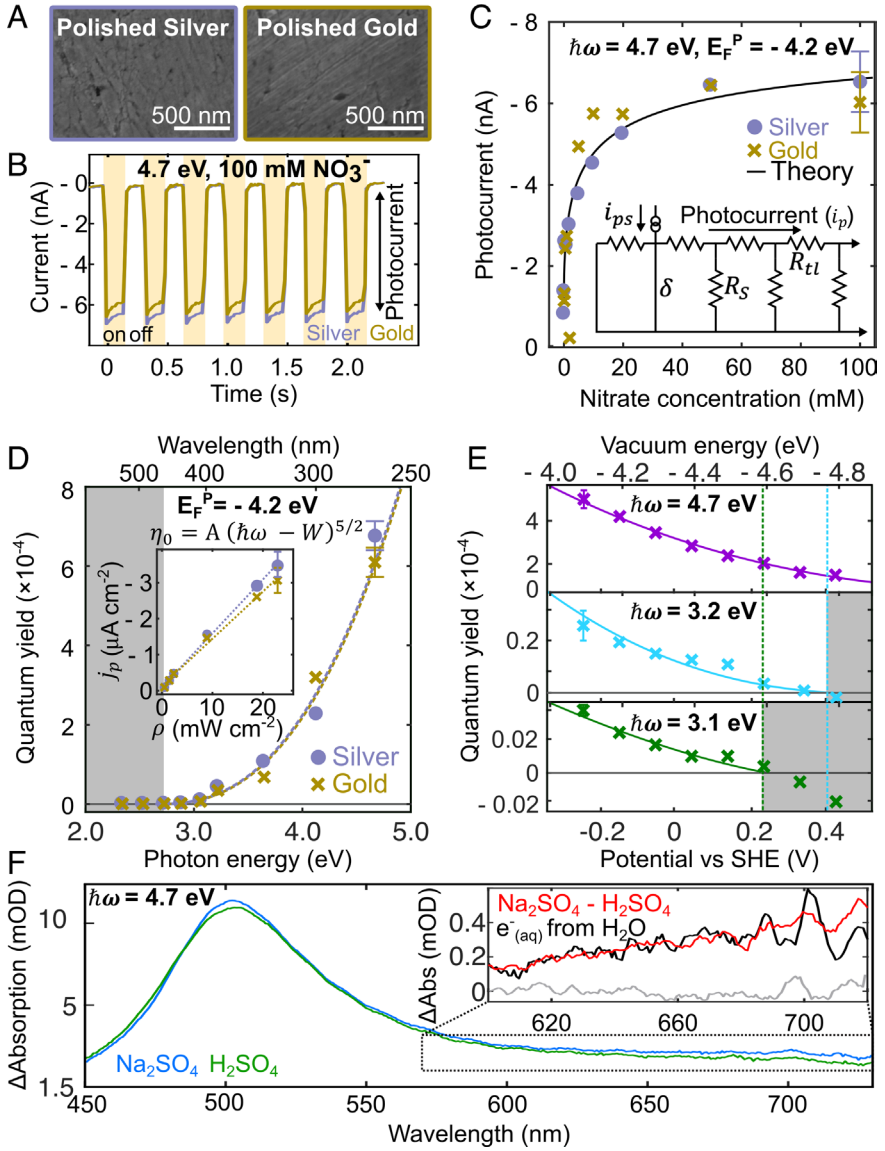

Fig. 2. Electron photoemission in the absence of plasmon excitation. (*A*) SEM of polished silver and gold electrodes, exhibiting no defined nanoscale features. (*B*) Current collected as a function of time with modulated 4.7 eV illumination (23 μW cm^{-2}) from an LED. For electrochemical measurements the supporting electrolyte was $NaClO_4$. (*C*) Dependence of photocurrent on electron scavenger concentration compared to an equivalent circuit model (*SI Appendix*, Fig. S1) (40), which treats photoemission as injection of a current, i_{ps}, into a transmission line circuit at a deposition plane δ, followed by motion along series resistors, R_{tl}, and homogenous capture of electrons by scavengers (R_S). The error bars represent SE. (*D*) Photoemission spectra (data points) for polished electrodes in 100 mM NO_3^- and fit (line) to Eq. **1**. Photon energies below the threshold are indicated by the shaded area. *Inset*: photocurrent, j_p, dependence on 4.7 eV illumination power density, ρ. (*E*) Photoemission yield for a gold electrode as a function of applied potential. Solid lines are fits to Eq. **1**. Dashed vertical lines and shaded areas indicate the potentials above which E_F^P was too low for photoemission to occur at $\hbar\omega$ = 3.2 eV and $\hbar\omega$ = 3.1 eV. The small negative values for 3.2 eV and 3.1 eV illumination are artifacts resulting from anodic electrode charging (*SI Appendix*, Fig. S2). (*F*) Ultrafast transient absorption spectra of a polished gold electrode in an inert electrolyte (Na_2SO_4) and after adding acid (H_2SO_4) as an electron scavenger, pumped at 4.7 eV and probed at a delay time of 1,200 ps. Na_2SO_4 was used here to avoid two-photon ionization of $NaClO_4$. The main signal, peaked near 500 nm, is due to electronic transitions in gold, while the characteristic solvated electron absorption at 700 nm is visible by the difference between spectra with and without acid, as highlighted in the *Inset*, which includes a solvated electron spectrum obtained from two-photon ionization of water only and scaled for comparison. The difference signal was clearly above the background noise, as indicated by the gray line that corresponds to the transient absorption without pump. In fact, the noise of the background, obtained by evaluating its standard deviation, was 0.02 mO, an order of magnitude lower than the signal (see *SI Appendix*, Figs. S6–S10 for further details).

W is the threshold photon energy (Fig. 1 *A* and *B*). Spectrally resolved quantum yields, obtained from measured photocurrents and incident light intensities as a function of excitation wavelength under the same conditions as in Fig. 2*B*, are in excellent agreement with Eq. **2**. A 5/2 power law fit of η_0 vs. $\hbar\omega$ revealed a threshold of 2.7 eV for gold and silver, matching the expected energy gap for a one-photon process between the applied potential controlled electrode Fermi level (–4.2 eV) and the electron injection level in water (–1.5 eV) (Fig. 2*D*) (21, 41). The fact that the threshold photon energy is determined by the applied electrochemical potential was further verified by recording quantum yields at constant photon energies while varying the electrode potential (Fig. 2*E*). Finally, the optical detection of solvated electrons based on their characteristic absorption (42) excluded the possibility that the scavengers reacted directly at the electrode surface (Fig. 2*F* and *SI Appendix*, Fig. S10). Furthermore, the quantum yield of solvated electron generation calculated from the transient absorption signal was 3×10^{-3}, comparable to the value measured by electrochemical detection (*SI Appendix*, Fig. S10).

After verifying solvated electron generation from polished electrodes, we found that plasmon excitation enhances photoemission from nanostructured electrodes. Solvated electron yields slightly increased for electrochemically roughened silver electrodes (Fig. 3*A*), consistent with previous work (17, 43). However, the addition of 95 nm colloidal nanoparticles with well-defined localized plasmons resulted in a stronger enhancement for silver (Fig. 3*B*), while equivalent nanostructuring of the gold electrode had no effect (Fig. 3*C*). The improved shape and size control of colloidally synthesized nanoparticles importantly enabled us to model electric fields and hot carrier distributions.

Spectrally resolved photoemission enhancement factors, obtained from the ratio of photoemission yields between nanostructured and polished electrodes (Fig. 3*D*), revealed maxima in photoemission enhancement for both nanostructured silver electrodes at a photon energy of 3.2 eV, equal to the silver nanoparticle plasmon resonance (Fig. 3 *D*, *Inset* and *SI Appendix*, Fig. S18). We therefore assign the origin of the observed photoemission enhancement to the nanostructured features that support localized surface plasmons. Importantly, this interpretation is consistent with the absence of enhancement for the gold nanoparticle-decorated electrode because the plasmon for gold spheres peaks at ~2.5 eV, below the photon energy threshold of 2.7 eV at E_F^P = −4.2 eV. Consistent with a one-photon process, photoemission enhancement scaled linearly with illumination power when a silver nanoparticle-decorated electrode was illuminated on resonance. Based on the negligible effect of lattice heating on electron temperature and our observed linear power dependence, we further rule out photothermal contributions to electron photoemission under our conditions (44) (*SI Appendix*, Fig. S19).

Modeling the plasmonic properties based on the actual electrode morphology showed that photoemission enhancement scales linearly with electric field enhancement, directly linking solvated electron generation to plasmon excitation. We used scanning electron microscopy (SEM) images of the nanostructured electrodes to simulate the local electric field enhancement (Fig. 4 *A*–*C*). Spectra of electric field enhancement, obtained by spatially averaging the internal electric field within a 10 nm region from the interface to account for the mean free path of the hot electrons, matched photoemission enhancement above the 2.7 eV threshold without the need for scaling (Fig. 4 *E* and *F*) (45). For the roughened silver electrode, the electric field enhancement was spatially averaged over a two-dimensional cross-sectional slice of the electrode as no clear boundaries between internal and external electric fields could be drawn, also yielding excellent agreement. All enhancements of one-photon photoemission yields follow a linear dependence on electric field enhancement (Fig. 4*G*), according to:

$$\eta_{nano} / \eta_0 \propto \left|E^2\right| / \left|E_0^2\right|. \quad [3]$$

η_{nano} represents the photoemission yields for the nanostructured electrodes. This linear correlation strongly suggests a hot electron-driven bulk photoemission process because plasmon-induced hot electron generation in nanoparticles scales with electric field enhancement (19, 46). This interpretation is in good agreement with vacuum photoemission studies of nanoparticles with similar electric field distributions (47). Based on the absence of photoemission enhancement for the nanostructured gold electrode, we furthermore exclude a surface photoemission process (Figs. 1*B* and 4*F*). If surface photoemission were occurring, the increase in surface area normal to the incident light for the gold nanoparticle-decorated electrode would favor this mechanism, even in the absence of plasmon excitation below threshold (16, 20). No photoemission enhancement was observed for the roughened gold electrode (*SI Appendix*, Fig. S20), further confirming this conclusion.It has been predicted that the injection

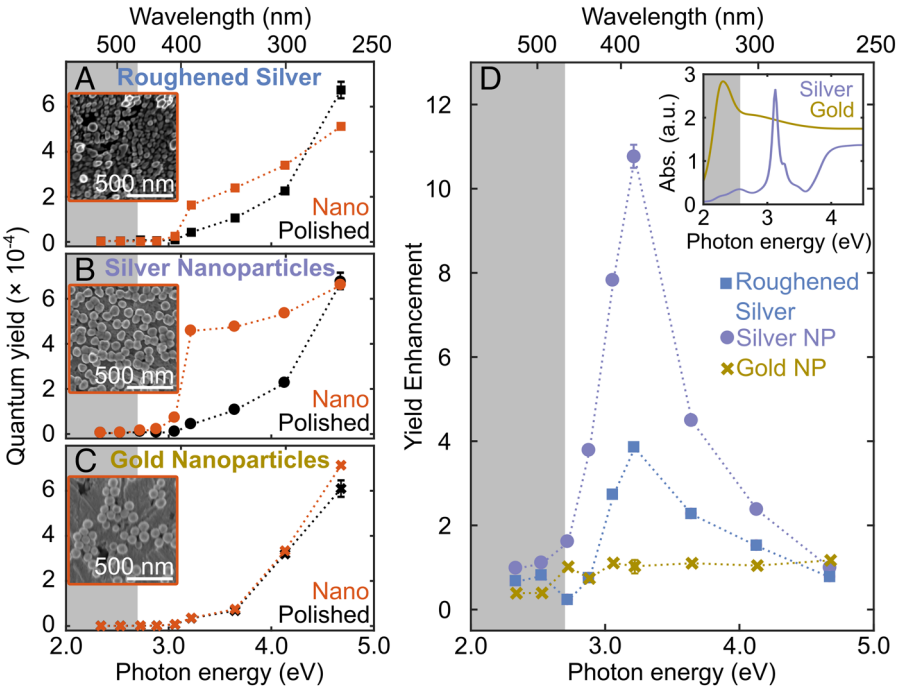

Fig. 3. Plasmon excitation enhances photoemission. (*A*–*C*) Photoemission spectra for polished compared to nanostructured electrodes at E_F^P = −4.2 eV in 100 mM NO_3^-. *Inset*: SEM characterization of the electrodes, which were found to be stable throughout the photocurrent measurements (*SI Appendix*, Fig. S11). Further characterization is given in *SI Appendix*, Figs. S12–S19. (*D*) Quantum yield enhancement for the electrodes shown in *A*–*C*. *Inset*: Mie theory simulated absorption spectra of 95 nm silver and gold nanospheres, demonstrating the spectral positions of the corresponding dipolar plasmon resonances. Photon energies below the photoemission threshold are indicated by shaded areas.

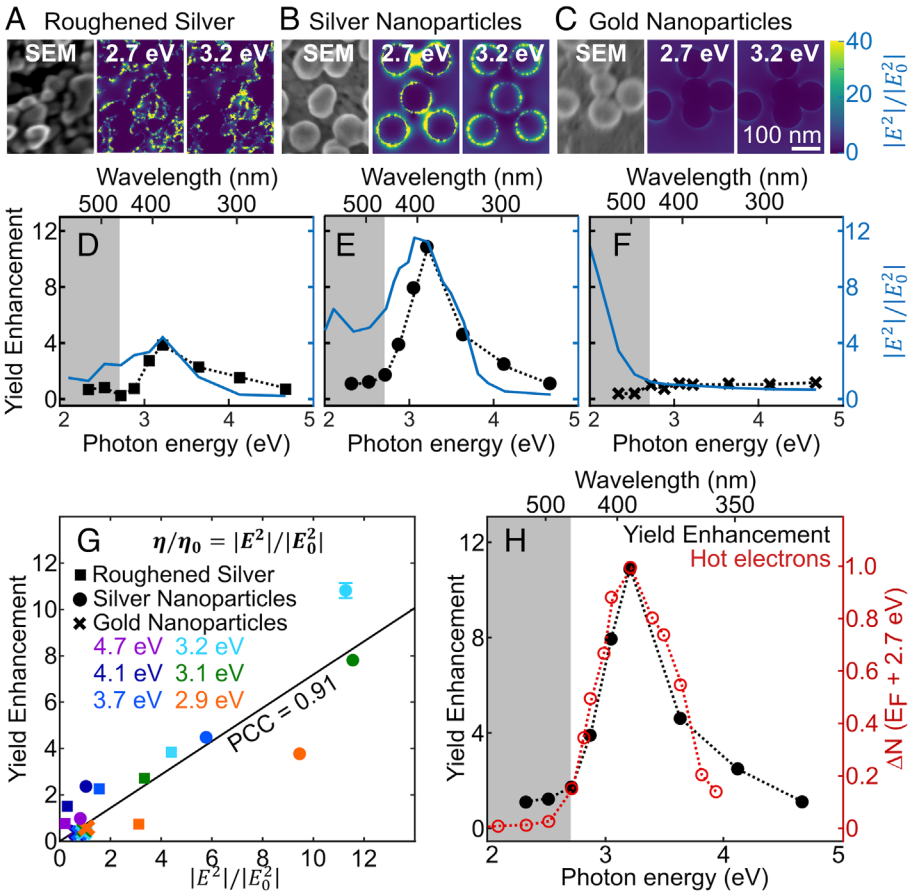

Fig. 4. Electron photoemission is driven by plasmon-induced hot carriers. (*A*–*C*) SEM micrographs and electric field enhancement maps of representative areas for the different nanostructured electrodes, with further analysis given in *SI Appendix*, Fig. S25. (*D*) Spatially averaged electric field enhancement for the electrode area pictured in *A* for a 2D cross-section through the roughened electrode plane (blue line). (*E* and *F*) Volume average of the internal electric field within a 10 nm skin depth of the nanoparticle, equal to the mean free path of a 2.7 eV electron (blue lines). Overlaid in *E* and *F* are the enhancement spectra from Fig. 3*D* (black). Changes in plasmon resonance due to charging of the metal electrode were negligible (*SI Appendix*, Fig. S26). Lower yield enhancements than expected based on simulated electric field enhancements at the highest photon energies could be due to a change in hot carrier distribution following interband excitations (45). (*G*) Photoemission enhancement as a function of electric field enhancement for all data points in *D*–*F* with photon energies above threshold, i.e., >2.7 eV. The black line indicates a linear correlation with a Pearson correlation coefficient (PCC) of 0.91. (*H*) Simulated normalized change in distribution ΔN of hot electrons with energies 2.7 eV or more above the Fermi level (red line), calculated using the electric field shown in *E*, in comparison to the corresponding experimental photoemission yield enhancement spectrum (black).

efficiency of hot electrons from plasmonic nanostructures into semiconductors following a bulk process can be enhanced by local roughness if feature sizes are just a few nanometers or smaller (48). However, atomic force microscopy (AFM) of both polished and electrochemically roughed electrodes revealed a significantly larger surface roughness on the order of 10 to 100 nm (*SI Appendix*, Fig. S15). Additional discussion of the photoemission mechanism is given in *SI Appendix*, Table S5.

Simulations of the hot carrier distributions in a silver nanosphere confirmed the proposed hot electron-driven mechanism. Although coupling among neighboring nanoparticles and with the metal electrode creates larger field enhancements ($|E^2|/|E_0{}^2| = 31$), these coupled modes have energies below 2.7 eV, making the single-particle resonance the only relevant plasmon mode for the silver nanoparticle-decorated electrode (Fig. 4*E* and *SI Appendix*, Figs. S21–S24). Additionally, given the large size of the nanoparticles, the electron wavefunctions are nearly independent of the boundary conditions. We therefore calculated the distribution of hot electrons in a single silver particle but using an internal field that was calculated from the average of internal fields simulated for the nanoparticle-decorated electrode (Fig. 4*B*) (45, 49, 50). The electrons in the nanoparticle were treated as electrons in a three-dimensional box, and hot carrier distributions were simulated by perturbing the electrons using this average internal electric field. All electrons above the 2.7 eV photoemission threshold and within a distance of 10 nm from the surface were summed, based on their volume fraction with the assumption of a uniform free electron distribution. This simulated hot electron distribution matched well with the experimental photoemission yield enhancement and reproduced a maximum at 3.2 eV (Fig. 4*H*). An estimate of the external quantum efficiency for hot electron generation also exhibited a peak at 3.2 eV (*SI Appendix*, Fig. S27) with a value of 2.2×10^{-3}, compared to a measured quantum yield of 4.5×10^{-4}, implying that about 20% of all hot carriers become solvated electrons. The close agreement among the calculated hot electron distribution, the simulated electric field, and the experimental photoemission enhancement spectrum for the nanoparticle-decorated silver electrode establishes the so-far missing mechanistic connection between solvated electron generation from roughened metal electrodes and plasmon excitation.

Conclusion

In summary, we demonstrated that under mild, continuous-wave illumination, hot carriers generated from plasmon decay can inject

into surrounding solutions where they form solvated electrons (Fig. 1*A*). Through a careful combination of electrochemical and spectroscopic detection as well as many control experiments, we were able to rule out other important effects such as photothermal heating, electrode charging, and electrode surface reactions and find that our data is only consistent with photoemission of electrons into solution. Although photoemission yields are low, optimized nanostructures support 1,000-fold larger electric field enhancements on the order of 40,000 at sharp tips or in nanoscale gaps (51, 52). In comparison, the first proof-of-principle external quantum efficiencies for plasmon-aided heterogeneous catalysis were on the order of 10^{-6} to 10^{-3} (33, 53) and have since been improved by 10 to 100 times (25, 54). One approach to extend hot electron lifetimes and hence efficiencies is via charge injection into an adjacent semiconductor such as TiO_2 where carrier lifetimes are on the order of 100 ps (55). In comparison, solvated electrons have a lifetime of 160 ns and can even reach 100 μs if aqueous solutions are properly purged of scavengers like O_2 and CO_2 (56).

To increase photoemission yields, optimized electric fields can be tuned to photon energies above the threshold by varying the plasmonic metal, solvent, and electrolyte, as we have shown here that their combination dictates the plasmon energy, intrinsic Fermi level, solvated electron energy, and applied potential range free from interfering redox chemistry. A possible strategy toward larger yields is the fabrication of coupled nanostructures from the sustainable metal aluminum with its higher energy plasmon modes, and the use of an aprotic solvent (51, 52, 57, 58). Also, changing to a surface photoemission mechanism by reducing the nanoparticle size is expected to increase yields by 10-fold as fast internal relaxation of the hot electrons is circumvented (16, 36, 59). Our conditions are therefore among the most difficult, but at the same time most historically relevant, because parallels between photoemission and SERS at the same roughened electrodes were initially posed (60), but never investigated fully. Considering the evolution of SERS, we expect that we can similarly turn an apparent flaw (an irregular electrode) into a desirable feature for solvated electron generation based on the mechanistic insight developed here and the ability to tailor electric fields with plasmons, with additional guidance from theoretical studies on the efficiencies of the elementary steps involved.

Materials and Methods

Chemicals. $NaNO_3$ (>99.0% pure, Sigma Aldrich), $NaClO_4$ (>98.0% pure, Sigma Aldrich), NaCl (biological grade, Fischer Scientific), H_2SO_4 (99.9999% pure, Alfa Aesar), and Na_2SO_4 (99.9955% pure, Alfa Aesar) were used as received and diluted in Millipore water (>1 MΩ resistivity). $NaNO_3$ and H_2SO_4 were used as scavengers, $NaClO_4$ for electrochemical roughening and as a background electrolyte, and NaCl and Na_2SO_4 as background electrolytes. Colloidally synthesized nanoparticles (100 nm BioPure Silver Nanospheres, Nanocomposix, and 100 nm BioPure Gold, Nanocomposix) were concentrated by centrifuging 1.5 mL of nanosphere solution at 10,000 rpm for 10 min. 1 mL of supernatant was decanted off and the nanoparticles were redispersed in the remaining supernatant by sonication for 2 min. SEM revealed that the actual sizes were 95 nm and 94 nm for the silver and gold nanospheres, respectively (*SI Appendix*, Fig. S16).

Gold and Silver Films. Gold films were fabricated via electron beam evaporation by deposition of a 2-nm titanium adhesion layer followed by a 30-nm gold film at a deposition rate of 0.3 to 0.5 Å s^{-1}. Silver films were fabricated via electron beam evaporation by deposition of a 100-nm silver film at a deposition rate of 0.3 to 0.5 Å s^{-1}.

Electrode Preparation. L-shaped electrodes were fabricated by embedding 0.5 mm gold or silver wire (99.99%, Goodfellow) in epoxy surrounded by a bent glass tube and polished using sandpaper, 300 μm alumina powder, and 50 μm alumina powder. Electrochemically roughened silver electrodes were prepared using three cyclic voltammetry (CV) scans between –0.27 and 1.14 V vs. standard hydrogen electrode (SHE) at a scan rate of 1 V s^{-1} in 100 mM $NaClO_4$, starting and ending at –0.27 V. After roughening, the electrode was then held at –0.27 V for 1 min to ensure all $AgClO_4$ was fully reduced. All potentials were measured vs. Ag/AgCl (1 M KCl) and converted to SHE. Nanoparticle-decorated electrodes were prepared by drop casting 25 μL of the concentrated nanoparticle solution onto a freshly polished gold or silver electrode. The electrode was then plasma cleaned under oxygen for 2 min to remove surface ligands and rinsed briefly with Millipore water (>1 MΩ resistivity). A freshly polished electrode yielded comparable photocurrents before and after plasma cleaning, concluding that plasma cleaning does not affect the photoemission properties.

Photocurrent Measurements. An L-shaped electrode was inserted into one opening of a 10-cm-path-length quartz cuvette with two openings (Starna). An Ag/AgCl (1 M KCl) reference electrode and a glassy carbon counter electrode (Alfa Aesar) were inserted into the other opening of the cuvette. The solution was degassed for 10 min using a glass tube connected to an argon tank (ultra-high purity grade, Airgas), after which the glass tube was raised to form a blanket of argon over the electrolyte solution. LEDs were focused onto the electrode surface using a collimating lens assembly (ThorLabs) followed by a quartz focusing lens (ThorLabs). An LED driver (ThorLabs) and potentiostat (CH Instruments 630E) were synchronized using a microcontroller (Arduino Uno) to initiate a current-time measurement with a sample rate of 60 Hz, while the LED was turned on and off at 6 Hz. Photocurrents were calculated by taking the difference between the average of the last five data points when the LED was on and the average of the first five data points when the LED was turned off again. This analysis was done only for the last 50 on–off steps, when the baseline of the current-time trace was nearly flat. Photocurrents, i_p, were converted into external quantum yields, η_0, using the measured incident light power, P, and the peak photon energy, $\hbar\omega$, of the LED according to Eq. **1** (see *SI Appendix*, Table S1 for LED powers). For visualization, current–time traces shown in Fig. 2 were background corrected by subtracting the value of the last data point from the entire trace, as typically done in the literature (61, 62). Fits to the 5/2-power law (Eq. **2**) were performed by a linear regression of ${\eta_0}^{2/5}$ against $\hbar\omega$ (for Fig. 2*D*) or E_F^P (Fig. 4*E*) as established previously (14, 44) (see *SI Appendix*, Table S2 for information about the fits). The power dependence was fitted using a linear regression of current vs. power density. All fits were performed using the "fitlm" function in MATLAB. Note that the electrode Fermi level was modified through the applied potential, and thus the intrinsic Fermi level of the metal (gold or silver) did not affect the energetics of photoemission (44). The symbol E_F^P is used throughout the manuscript to clarify that the Fermi level was modified by an applied electrochemical potential.

SEM. SEM imaging was carried out at 2 kV and 100 pA with a dwell time of 1 μs using a FEI Helios NanoLab 660 microscope.

Transient Absorption Spectroscopy. Transient absorption spectra of solvated electrons emitted from a gold film were collected on the 1.5 kHz repetition rate transient absorption setup, described in detail in *SI Appendix*. Briefly, a 266-nm pump pulse was generated using the third harmonic of an 800 nm, 4.5 mJ, 90 fs Ti:sapphire (Coherent Legend Elite Duo) fundamental pulse and passed through a 10-cm-long fused silica rod to lengthen the pulse in time from ~100 fs to 530 fs. Probe pulses with a spectral range extending from 450 to >750 nm were generated via self-phase modulation by passing a portion of the Ti:sapphire fundamental pulse through a c-cut sapphire window. The time delay between the arrival of the pump and probe pulses at the sample was adjusted via a computer-controlled delay stage (Newport ILS300LM) and spectra were collected using a charge-coupled device (CCD) camera (Princeton Instruments PyLoN 100BR) connected to a spectrometer (Acton Instruments SP2500 SpectraPro 2556-i).

Finite-Difference Time Domain (FDTD) Simulations. FDTD simulations of nanostructured electrodes were carried out using the commercial software package Lumerical FDTD Solutions to obtain electromagnetic field distributions and absorption cross sections. The geometric model for roughened electrodes was established based on topographic information from SEM micrographs, which were converted into binary images and then imported into the FDTD software (26). Nanospheres with a diameter of 95 nm were used for modeling nanoparticle-decorated electrodes. SEM micrographs were still imported and used as a guide

to mimic the exact configurations of nanoparticles on the electrodes. For each arrangement, the interparticle separations between nanospheres were varied within 1 to 5 nm to ensure calculated properties were not restricted to a specific configuration. All these structures were simulated sitting on a semi-infinite gold or silver substrate submerged in water. The dielectric function for gold and silver was extracted from values measured by Johnson and Christy (63). The computational mesh size was set to 1 nm for all simulations. A total field scattering field light source was propagated along the z-axis, and two perpendicular polarizations were used for illumination to simulate unpolarized light. Default convergence criteria were used for all the simulations, i.e., the energy remaining in the simulation region as a fraction of the power injected into the simulation needs to fall below a 10^{-7} threshold. Perfectly matched layers surrounded the structures to avoid reflections from the boundaries.

Mie Theory Simulations. Mie theory simulations were carried out using a modified version of the MatScat functions (Copyright 2016, Jan Schäfer) (64) with dielectric values from Johnson and Christy (63). The refractive index of the medium was set to 1.33 for water.

Calculations of Hot Carrier Distributions. The hot carrier population was calculated for a silver sphere with a diameter of 95 nm using the approach described in ref. 50. The conduction electrons within the silver nanoparticle were treated as free electrons with number density of 5.86×10^{28} m^{-3} confined to an infinite potential well to calculate the Fermi energy. Given the large size of the nanoparticles, the electron wavefunctions are nearly independent of the boundary conditions. We therefore approximated the electron wavefunctions in the spherical nanoparticle with the wavefunctions of a particle in a three-dimensional box with length, $L = 95$ nm, according to:

$$\Psi_n = \sqrt{\frac{2^3}{L^3}} \sin(\pi n_x x/L) \sin(\pi n_y y/L) \sin(\pi n_z z/L) \qquad [4]$$

n_x, n_y *and* $n_z = 1, 2, 3, \ldots$ are quantum numbers. The volume-averaged electric field, E, inside the spherical nanoparticle upon uniform illumination was determined from the FDTD simulation of the electrode pictured in Fig. 4*B*. The electric field within 10 nm from the interface, equal to the mean free path of a hot electron 2.7 eV above the Fermi level (45), was volume-averaged for all five particles. We chose this approach because the model cannot be applied to a collection of multiple particles. However, as the internal fields below photoemission threshold are dominated by the single-particle resonance, using an averaged field of multiple particles on a substrate provided the closest possible representation of a nanoparticle-decorated electrode. The incident photon excitation with frequency, ω, was treated as a first-order perturbation and the resulting change in electron population, $\delta\rho_{nn'}$ for a state n was calculated using Fermi's Golden Rule:

$$\delta\rho_{nn} = 4e^2 \sum_{n'} \left(f^0_{n'} - f^0_n\right) \left|\phi_{nn'}\right|^2 \times \left\{ \frac{1}{\left(\hbar\omega - E_n + E_{n'}\right)^2 + \Gamma^2} + \frac{1}{\left(\hbar\omega + E_n - E_{n'}\right)^2 + \Gamma^2} \right\} \qquad [5]$$

where e is the electron charge, f^0 is the equilibrium Fermi–Dirac distribution, Γ is the energy broadening, E_n is the energy of the nth level, and $\phi_{nn'} = \langle n \,|\, \phi \,|\, n' \rangle$ is the matrix element for the excitation from level n' to n due to the induced potential $\phi(r) = zE(\omega)$ inside the nanoparticle (49, 65). The energy broadening term was taken to be equal to the Drude damping rate, $\Gamma = 0.06$ eV (65). The number of hot electrons, ΔN, produced with energies greater than the 2.7 eV photoemission threshold was calculated for incident photon energies between 1 and 4 eV:

$$\Delta N\left(E_F + 2.7eV\right) = \sum_{E_n \geq \left(E_F + 2.7eV\right)} \delta\rho_{nn} \qquad [6]$$

Hot carrier distributions were only calculated up to 4 eV as the model does not capture the effect of interband transitions.

Data, Materials, and Software Availability. Raw data have been deposited in plasmons generate solvated electrons (Al-Zubeidi, Link) (https://rice.box.com/s/4tmqaubp6dnar1d67eez5f8lu42icmg0).

ACKNOWLEDGMENTS. We thank K.A. Willets for helpful discussions and the Rice University Shared Equipment Authority and Electron Microscopy Center for instrument use. C.C.C. thanks Harsha Reddy for discussions regarding calculations of hot carrier distributions. This work was funded by the NSF, Center for Adapting Flaws into Features (NSF CHE-2124983). S.A.L thanks the Robert A. Welch Foundation for support through the Charles W. Duncan, Jr.-Welch Chair in Chemistry (C-0002). C.F.L. acknowledges funding from the Robert A. Welch Foundation (C-1787). An acknowledgment is made to the donors of the American Chemical Society Petroleum Research Fund for partial support of this research to S.L. (62665-ND6).

Author affiliations: [a]Department of Chemistry, Rice University, Houston, TX 77005; [b]Center for Adapting Flaws into Features, Rice University, Houston, TX 77005; [c]Department of Electrical and Computer Engineering, Rice University, Houston, TX 77005; [d]Department of Applied Physics, Stanford University, Stanford, CA 94305; [e]Department of Chemistry, University of Texas at Austin, Austin, TX 78712; [f]Department of Materials Science and Engineering, Stanford University, Stanford, CA 94305; [g]Department of Radiology, Stanford University, Stanford, CA 94305; and [h]Department of Chemical and Biomolecular Engineering, Rice University, Houston, TX 77005

1. W. A. Alexander, J. P. Wiens, T. K. Minton, G. M. Nathanson, Reactions of solvated electrons initiated by sodium atom ionization at the vacuum-liquid interface. *Science* **335**, 1072–1075 (2012).
2. B. K. Peters *et al.*, Scalable and safe synthetic organic electroreduction inspired by Li-ion battery chemistry. *Science* **363**, 838–845 (2019).
3. A. J. Birch, S. M. Mukherji, Reduction by sodium - ammonia solutions. *Nature* **163**, 766–766 (1949).
4. R. Hawtof *et al.*, Catalyst-free, highly selective synthesis of ammonia from nitrogen and water by a plasma electrolytic system. *Sci. Adv.* **5**, eaat5778 (2019).
5. D. Zhu, L. Zhang, R. E. Ruther, R. J. Hamers, Photo-illuminated diamond as a solid-state source of solvated electrons in water for nitrogen reduction. *Nat. Mater.* **12**, 836–841 (2013).
6. R. Naumann, F. Lehmann, M. Goez, Generating hydrated electrons for chemical syntheses by using a green light-emitting diode (LED). *Angew. Chem. Int. Ed.* **57**, 1078–1081 (2018).
7. Y. Dong, D. Parobek, D. Rossi, D. H. Son, Photoemission of energetic hot electrons produced via up-conversion in doped quantum dots. *Nano Lett.* **16**, 7270–7275 (2016).
8. D. Solti *et al.*, Plasmon-generated solvated electrons for chemical transformations. *J. Am. Chem. Soc.* **144**, 20183–20189 (2022).
9. M. Cybularczyk-Cecotka, J. Szczepanik, M. Giedyk, Photocatalytic strategies for the activation of organic chlorides. *Nat. Catal.* **3**, 872–886 (2020).
10. M. V. Pavliuk *et al.*, Hydrated electron generation by excitation of copper localized surface plasmon resonance. *J. Phys. Chem. Lett.* **10**, 1743–1749 (2019).
11. K. Onda *et al.*, Wet electrons at the H_2O/TiO_2(110) surface. *Science* **308**, 1154–1158 (2005).
12. J. P. Cole *et al.*, Organocatalyzed birch reduction driven by visible light. *J. Am. Chem. Soc.* **142**, 13573–13581 (2020).
13. B. C. Garrett *et al.*, Role of water in electron-initiated processes and radical chemistry: Issues and scientific advances. *Chem. Rev.* **105**, 355–390 (2005).
14. Y. V. Pleskov, Z. A. Rotenberg, Regularities of photoemission from metals into electrolyte solutions. *J. Electroanal. Chem. Interf. Electrochem.* **20**, 1–12 (1969).
15. J. K. Sass, R. K. Sen, E. Meyer, H. Gerischer, Effect of surface plasmon excitation on photoemission and photooxidation processes at a silver-electrolyte interface. *Surf. Sci.* **44**, 515–528 (1974).
16. M. Graf *et al.*, Surface-to-volume ratio drives photoelelectron injection from nanoscale gold into electrolyte. *ACS Catal.* **9**, 3366–3374 (2019).
17. R. Kostecki, J. Augustynski, Effect of the surface roughness on the spectral distribution of photoemission current at the silver/solution contact. *Int. J. Appl. Phys.* **77**, 4701–4705 (1995).
18. Y. Wu *et al.*, SERS study of the mechanism of plasmon-driven hot electron transfer between gold nanoparticles and PCBM. *J. Phys. Chem. C* **123**, 29908–29915 (2019).
19. E. Cortés *et al.*, Plasmonic hot electron transport drives nano-localized chemistry. *Nat. Commun.* **8**, 14880 (2017).
20. J. B. Khurgin, A. Petrov, M. Eich, A. V. Uskov, Direct plasmonic excitation of the hybridized surface states in metal nanoparticles. *ACS Photonics* **8**, 2041–2049 (2021).
21. J. Stähler *et al.*, Real-time measurement of the vertical binding energy during the birth of a solvated electron. *J. Am. Chem. Soc.* **137**, 3520–3524 (2015).
22. L. Turi, W.-S. Sheu, P. J. Rossky, Characterization of excess electrons in water-cluster anions by quantum simulations. *Science* **309**, 914–917 (2005).
23. F. Lapointe, M. Wolf, R. K. Campen, Y. Tong, Probing the birth and ultrafast dynamics of hydrated electrons at the gold/liquid water interface via an optoelectronic approach. *J. Am. Chem. Soc.* **142**, 18619–18627 (2020).
24. R. E. Larsen, W. J. Glover, B. J. Schwartz, Does the hydrated electron occupy a cavity? *Science* **329**, 65–69 (2010).
25. L. Zhou *et al.*, Quantifying hot carrier and thermal contributions in plasmonic photocatalysis. *Science* **362**, 69–72 (2018).
26. D. M. Solís *et al.*, Toward ultimate nanoplasmonics modeling. *ACS Nano* **8**, 7559–7570 (2014).
27. G. V. Hartland, Optical studies of dynamics in noble metal nanostructures. *Chem. Rev.* **111**, 3858–3887 (2011).

28. Q. Zhang *et al.*, Unraveling the origin of chirality from plasmonic nanoparticle-protein complexes. *Science* **365**, 1475–1478 (2019).
29. E. Ponomareva, K. Volk, P. Mulvaney, M. Karg, Surface lattice resonances in self-assembled gold nanoparticle arrays: Impact of lattice period, structural disorder, and refractive index on resonance quality. *Langmuir* **36**, 13601–13612 (2020).
30. P. Z. El-Khoury, Z. D. Schultz, From SERS to TERS and beyond: Molecules as probes of nanoscopic optical fields. *J. Phys. Chem. C* **124**, 27267–27275 (2020).
31. M. J. Horton *et al.*, Nanoscopy through a plasmonic nanolens. *Proc. Natl. Acad. Sci. U.S.A.* **117**, 2275–2281 (2020).
32. K. Sytwu *et al.*, Driving energetically unfavorable dehydrogenation dynamics with plasmonics. *Science* **371**, 280–283 (2021).
33. S. Mubeen *et al.*, An autonomous photosynthetic device in which all charge carriers derive from surface plasmons. *Nat. Nanotechnol.* **8**, 247–251 (2013).
34. Y. Kim, J. G. Smith, P. K. Jain, Harvesting multiple electron–hole pairs generated through plasmonic excitation of Au nanoparticles. *Nat. Chem.* **10**, 763–769 (2018).
35. H. Nakanishi *et al.*, Photoconductance and inverse photoconductance in films of functionalized metal nanoparticles. *Nature* **460**, 371–375 (2009).
36. K. Wu, J. Chen, J. R. McBride, T. Lian, Efficient hot-electron transfer by a plasmon-induced interfacial charge-transfer transition. *Science* **349**, 632–635 (2015).
37. M. W. Knight, H. Sobhani, P. Nordlander, N. J. Halas, Photodetection with active optical antennas. *Science* **332**, 702–704 (2011).
38. M. Aeschlimann *et al.*, Coherent two-dimensional nanoscopy. *Science* **333**, 1723–1726 (2011).
39. J. Pettine *et al.*, Plasmonic nanostar photocathodes for optically-controlled directional currents. *Nat. Commun.* **11**, 1367 (2020).
40. G. C. Barker, A. W. Gardner, D. C. Sammon, Photocurrents produced by ultraviolet irradiation of mercury electrodes. *J. Electrochem. Soc.* **113**, 1182 (1966).
41. C. E. Krohn, P. Antoniewicz, J. Thompson, Energetics for photoemission of electrons into NH3 and H2O. *Surf. Sci.* **101**, 241–250 (1980).
42. J. R. Casey, R. E. Larsen, B. J. Schwartz, Resonance Raman and temperature-dependent electronic absorption spectra of cavity and noncavity models of the hydrated electron. *Proc. Natl. Acad. Sci. U.S.A.* **110**, 2712–2717 (2013).
43. M. Fedurco, V. Shklover, J. Augustynski, Effect of halide ion adsorption upon plasmon-mediated photoelectron emission at the silver/solution interface. *J. Phys. Chem. B* **101**, 5158–5165 (1997).
44. A. M. Brodsky, Y. V. Pleskov, Electron photoemission at a metal-electrolyte solution interface. *Prog. Surf. Sci.* **2**, 1–73 (1972).
45. M. Bernardi, J. Mustafa, J. B. Neaton, S. G. Louie, Theory and computation of hot carriers generated by surface plasmon polaritons in noble metals. *Nat. Commun.* **6**, 7044 (2015).
46. R. Sundararaman *et al.*, Theoretical predictions for hot-carrier generation from surface plasmon decay. *Nat. Commun.* **5**, 5788 (2014).
47. J. Pettine *et al.*, Controlling the spatial and momentum distributions of plasmonic c arriers: Volume *vs* surface effects. *ACS Nano* **15**, 1566–1578 (2021).
48. M. Grajower, U. Levy, J. B. Khurgin, The role of surface roughness in plasmonic-assisted internal photoemission Schottky photodetectors. *ACS Photonics* **5**, 4030–4036 (2018).
49. G. V. Naik, J. A. Dionne, Photon upconversion with hot carriers in plasmonic systems. *Appl. Phys. Lett.* **107**, 133902 (2015).
50. A. O. Govorov, H. Zhang, Y. K. Gun'ko, Theory of photoinjection of hot plasmonic carriers from metal nanostructures into semiconductors and surface molecules. *J. Phys. Chem. C* **117**, 16616–16631 (2013).
51. M. B. Ross, G. C. Schatz, Aluminum and indium plasmonic nanoantennas in the ultraviolet. *J. Phys. Chem. C* **118**, 12506–12514 (2014).
52. D. O. Sigle, E. Perkins, J. J. Baumberg, S. Mahajan, Reproducible deep-UV SERRS on aluminum nanovoids. *J. Phys. Chem. Lett.* **4**, 1449–1452 (2013).
53. T. Oshikiri, K. Ueno, H. Misawa, Plasmon-induced ammonia synthesis through nitrogen photofixation with visible light irradiation. *Angew. Chem. Int. Ed.* **53**, 9802–9805 (2014).
54. X. Cai *et al.*, Ultrafast charge separation for full solar spectrum-activated photocatalytic H2 generation in a black phosphorus–Au–CdS heterostructure. *ACS Energy Lett.* **3**, 932–939 (2018).
55. L. Du, X. Shi, G. Zhang, A. Furube, Plasmon induced charge transfer mechanism in gold-TiO2 nanoparticle systems: The size effect of gold nanoparticle. *Int. J. Appl. Phys.* **128**, 213104 (2020).
56. B. F. Bachman *et al.*, Detection of aqueous solvated electrons produced by photoemission from solids using transient absorption measurements. *ACS Meas. Sci. Au* **2**, 46–56 (2022).
57. K. Itaya, R. E. Malpas, A. J. Bard, Photoelectron emission from a metal electrode in liquid ammonia. *Chem. Phys. Lett.* **63**, 411–415 (1979).
58. K. Murakoshi, K. Uosaki, Estimation of the relaxation energy of solvated electrons in hexamethylphosphoric triamide solution from photon emission measurements. *J. Electroanal. Chem. Interf. Electrochem.* **308**, 351–356 (1991).
59. A. V. Uskov *et al.*, Internal photoemission from plasmonic nanoparticles: Comparison between surface and volume photoelectric effects. *Nanoscale* **6**, 4716–4727 (2014).
60. C. W. Kim, J. C. Villagrán, U. Even, J. C. Thompson, Adsorbate effects on photoemission from Ag. *J. Chem. Phys.* **94**, 3974–3977 (1991).
61. K. P. Sokol *et al.*, Bias-free photoelectrochemical water splitting with photosystem II on a dye-sensitized photoanode wired to hydrogenase. *Nat. Energy* **3**, 944–951 (2018).
62. S. Szewczyk, R. Białek, G. Burdziński, K. Gibasiewicz, Photovoltaic activity of electrodes based on intact photosystem I electrodeposited on bare conducting glass. *Photosynth. Res.* **144**, 1–12 (2020).
63. P. B. Johnson, R. W. Christy, Optical constants of the noble metals. *Phys. Rev. B* **6**, 4370–4379 (1972).
64. J. Schäfer, S. C. Lee, A. Kienle, Calculation of the near fields for the scattering of electromagnetic waves by multiple infinite cylinders at perpendicular incidence. *J. Quant. Spectrosc. Radiat. Transf.* **113**, 2113–2123 (2012).
65. J. G. Liu, H. Zhang, S. Link, P. Nordlander, Relaxation of plasmon-induced hot carriers. *ACS Photonics* **5**, 2584–2595 (2018).